



Brillouin optical time-domain reflectometry using up-conversion single-photon detector



Haiyun Xia ^{a,b}, Mingjia Shangguan ^{c,d}, Guoliang Shentu ^{c,d}, Chong Wang ^a, Jiawei Qiu ^a, Mingyang Zheng ^e, Xiuping Xie ^e, Xiankang Dou ^{a,*}, Qiang Zhang ^{c,d,**}, Jian-Wei Pan ^{c,d}

^a CAS Key Laboratory of Geospace Environment, University of Science and Technology of China, Hefei, Anhui 230026, China

^b Collaborative Innovation Center of Astronautical Science and Technology, Harbin Institute of Technology, Harbin 150001, China

^c Shanghai Branch, National Laboratory for Physical Sciences at Microscale and Department of Modern Physics, University of Science and Technology of China, Shanghai 201315, China

^d Synergetic Innovation Center of Quantum Information and Quantum Physics, University of Science and Technology of China, Hefei, Anhui 230026, China

^e Shandong Institute of Quantum Science and Technology Co., Ltd, Jinan, Shandong 250101, China

ARTICLE INFO

Article history:

Received 4 May 2016

Received in revised form

3 June 2016

Accepted 18 June 2016

Keywords:

Brillouin optical time-domain reflectometry

Up-conversion

Single-photon detector

Fabry–Perot interferometer

ABSTRACT

A direct-detection Brillouin optical time-domain reflectometry (BOTDR) using an up-conversion photon-counting detector and an all-fiber structure Fabry–Perot scanning interferometer is demonstrated with shot-noise limited performance. Taking advantage of ultra-low noise equivalent power of the up-conversion photon-counting detector and high spectral resolution of the interferometer, the Brillouin spectra along a polarization maintaining fiber (PMF) are analyzed in the optical frequency domain directly. In contrast with heterodyne BOTDR, photon-counting BOTDR has better EM compatibility and faster speed in data processing. In experiments, using peak input power of 20 dBm, temperature profile along a 9 km PMF is retrieved according to the Brillouin shifts, with spatial/temporal resolution of 2 m/15 s. The precision is 0.7 °C at the leading end and 1.2 °C at the trailing end.

© 2016 Elsevier B.V. All rights reserved.

1. Introduction

For over two decades, distributed optical fiber sensors based on Brillouin scattering has attracted intensive interests, because it not only inherits features from common fiber sensors, such as durability, stability, small size, but also permits simultaneous temperature and strain detection in large infrastructures, aerospace industry, and geotechnical engineering [1].

These Brillouin-based distributed optical fiber sensors can mainly be divided into two types: the Brillouin optical time-domain analyzer (BOTDA) and Brillouin optical time-domain reflectometer (BOTDR). In the first type (BOTDA), a pulsed pump light is launched at one end of an optical fiber and interacts with the counterpropagating CW probe light injected from the other end. The probe light at Stokes (anti-Stokes) frequency is amplified (attenuated) by the pump light through the Brillouin gain (loss) process. By measuring the time dependent CW signal over a wide range of frequency difference between the pump and the probe, the Brillouin spectrum at each fiber location could be analyzed. To

increase the sensing length, the Brillouin loss regime is investigated rather than the gain regime [2]. In the second type (BOTDR), a pulsed light is launched into only one end of an optical fiber, and Brillouin backscattering is mixed with a reference light and heterodyne detection is performed at the optical coherent receiver. The Brillouin spectrum at any position along the optical fiber is measured by scanning the frequency difference between the local oscillation and the probe pulse [3]. The Stokes Brillouin signal is usually measured in BOTDR, since its power is generally higher than the anti-Stokes Brillouin signal [4].

Despite extensive research has been dedicated to improve the performance of Brillouin-based distributed optical fiber sensors, there are still some inherent drawbacks of the two mentioned popular techniques. As pointed out in the published works [5,6], BOTDA is best reserved for monitoring single large disturbance, which induces a Brillouin frequency shift greater than the Brillouin linewidth. Otherwise, the Brillouin gain spectrum at a specific point, from which one retrieves the temperature and strain values, is influenced by potential transfer of power between the pulsed pump light and the counterpropagating CW probe light along the fiber from the point where the pulse enters and the point under estimation. Fortunately, BOTDR overcomes this problem. But the traditional coherent detection scheme performed in the electrical domain results in a data-processing burden [7]. Furthermore,

* Corresponding author at: CAS Key Laboratory of Geospace Environment, University of Science and Technology of China, Hefei, Anhui 230026, China.

** Principle corresponding author.

E-mail addresses: dou@ustc.edu.cn (X. Dou), qiangzh@ustc.edu.cn (Q. Zhang).

coherent BOTDR usually works at the VHF (radio frequency from 30 MHz to 300 MHz), bringing out the EM compatible problem, for example, in the aircraft/spacecraft structural health and usage monitoring [8]. To resolve these challenges, a photon-counting BOTDR is proposed, which analyzes the Brillouin gain spectrum directly in the optical frequency domain. We noticed that distributed Brillouin sensors have been demonstrated by using a single-photon detector [9,10]. In the Rayleigh scattering BOTDA [9], to scan the Brillouin spectra along the fiber under test, a tunable high frequency microwave generator (about 10.8 GHz) is used to modulate the EOM, making the system sophisticated in electrical manipulation and sensitive to the EM interference. In the distributed Brillouin temperature sensor using a single-photon detector [10], only the intensity change of the Brillouin backscatter is monitored. In this paper, the Brillouin spectra along the fiber under test are scanned and reconstructed by using a high-resolution Fabry–Perot interferometer. At each distributed point, the whole information of the Brillouin spectrum: such as the frequency shift, bandwidth broadening, and power change can be interrogated for simultaneous temperature and strain detection.

As illustrated in Fig. 1, a novel photon-counting BOTDR incorporating up-conversion detector (UCD) and an all-fiber structure Fabry–Perot scanning interferometer (FFP-SI) is proposed. The Brillouin spectra along a sensing fiber are reconstructed directly from multiple backscattering traces collected by scanning the FFP-SI at different frequency relative to the Brillouin spectra. Since the backscattering traces are recorded and averaged on a multiscaler (multiple-event time digitizer) in photon-counting acquisition model (2-bit), the data volume is much smaller than the counterpart in coherent case (for example, a 14-bit analog to digital converter is used for sampling RF signal).

As the detector is considered, InGaAs avalanche photodiode (APD) is used for 1.5 μm detection usually. But it suffers from low efficiency (about 18%), high dark count rate (a few kilo-counts per second, cps) due to impurities and defects of the cathode material [11]. Superconducting single-photon detector (SSPD) at optical communication band has the advantages of high efficiency (>90%), ultralow noise (<1 cps), and low timing jitter (<100 cps) [12]. However, the requirement for liquid helium refrigeration equipment restricts their practical applications in many fields. Here, up-conversion technique is adopted to convert the Brillouin backscattering at 1.5 μm into NIR wavelength at 863 nm, which allows using Si APD instead of InGaAs APD with much better photon-counting characteristics, such as higher quantum

efficiency, lower dark count rate and less afterpulsing probability.

2. System

In the prototype system, the continuous wave from a seed laser (Keyopsys, PEFL-EOLA) is chopped into a pulse train after passing through an electro-optic intensity modulator (EOM) (Photline, MXER-LN-40 dB). The EOM is driven by an arbitrary waveform generator (Tektronix, AFG3102C), which determines the shape of the laser pulse and its repetition rate. The weak laser pulse is fed to a polarization maintaining EDFA (Amonics, AEDFA-PA-35), which deliver a pulse train with peak power of 20 dBm. The amplified spontaneous emission is filtered by using a fiber Bragg grating (FBG₁) in conjunction with a circulator (C₁).

Since the FFP-SI is a polarization sensitive device, a polarization maintaining fiber (PMF) is used instead of a single-mode fiber to mitigate the polarization fading problem. The backscattering signal along the PMF is coupled into the FFP-SI via the second circulator (C₂). An ultra-narrow FBG₂ in conjunction with the third circulator (C₃) is used to pick out the Brillouin signal against the strong Rayleigh signal component. To guarantee the system stability, the FFP-SI is cased in a temperature-controlled chamber.

As shown in Fig. 1, the continuous wave from the pump laser at 1950 nm is followed by a thulium-doped fiber amplifier, both manufactured by the AdValue Photonics (Tucson, AZ). The residual ASE noise is suppressed by using a 1.55/1.95 μm wavelength division multiplexer (WDM₁). The Brillouin backscattering from the sensing fiber and the pump laser are combined into a self-made periodically poled lithium niobate waveguide (PPLN-W) via the second WDM₂.

The so-called optimized quasi-phase matching condition is achieved by tuning the temperature of the PPLN-W, using a thermoelectric cooler [13]. The backscattering photons at 1548 nm are converted into sum-frequency photons at 863 nm and then picked out from the pump and spurious noise by using a series of filters, including a dichroic mirror, a short-pass filter (945 nm), a long-pass filter (785 nm) and a band-pass filter (863 nm) in cascade. Finally, the photons at 863 nm are focused onto a Si APD (EX-CELITAS, SPCM-AQRH-16). The TTL signal corresponding to the photons received is recorded on a multiscaler (FAST ComTec, MCS6A) and then transferred to a computer. In this work, by adjusting the pump power, the system detection efficiency of the UCD is tuned to 15%, with a dark noise level of 40 counts per second (cps), providing a noise equivalent power (NEP) about $8 \times 10^{-18} \text{ WHz}^{-1/2}$, which is one order lower than the value of Geiger-mode InGaAs/InP APD [14]. For reader's convenience, key parameters of the system are listed in Table 1.

3. Principle

The interaction between probe pulse and acoustic phonons generates Brillouin backscattering in an optical fiber. The phonons decay exponentially, so the Brillouin spectrum is Lorentzian in peak-normalized form [5]:

$$g_B(v) = g_0/[1 + (v - v_B)^2]/(\Delta v_B + \Delta v_L)^2 \quad (1)$$

where, within a limited dynamic range, Δv_B and v_B are demonstrated as linear functions of strain and temperature changes, respectively. $\Delta v_L = 0.44/\Delta t$ is the FWHM of an unchirped Gaussian pulse. Δt is the duration of the probe pulse, which determines the spatial resolution by $\Delta z = v\Delta t/2$, v is the group velocity of the lightwave in the sensing fiber.

The FFP-SI is fabricated with single-mode fiber with a

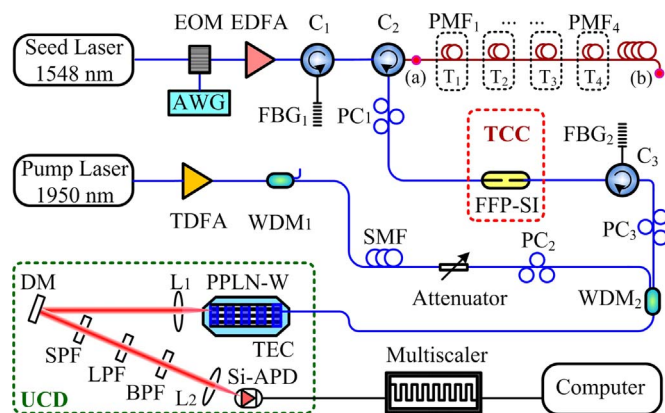


Fig. 1. System layout. EOM, electro-optic modulator; AWG, arbitrary waveform generator; EDFA, erbium doped fiber amplifier; C, circulator; PC, polarization controller; TCC, temperature controlled chamber; FFP-SI, fiber Fabry–Perot scanning interferometer; FBG, fiber Bragg grating; TDFA, thulium doped fiber amplifier; WDM, wavelength division multiplexer; SMF, single mode fiber; TEC, thermoelectric cooler; DM, dichroic mirror; SPF, short-pass filter; LPF, long-pass filter; and BPF, band-pass filter.

Table 1
Key parameters of the system.

Parameter	Value
Pulsed laser	
Wavelength (nm)	1548.1
Pulse duration (ns)	25.6
Peak power (mW)	100
Pulse repetition rate (kHz)	10
Pump laser	
Wavelength (nm)	1950
Power (mW)	300
FFP-SI	
Free spectrum range (GHz)	4.02
Full width at half-maximum (MHz)	93.5
Insert loss (dB)	2.25
PPLN waveguide	
QPM period (m)	20
Length (mm)	52
FWHM (nm)	0.3
Insert loss (dB)	1.4
Si: APD	
Detection efficiency at 863 nm (%)	45
Dark count (Hz)	9
Maximum count rate (MHz)	43

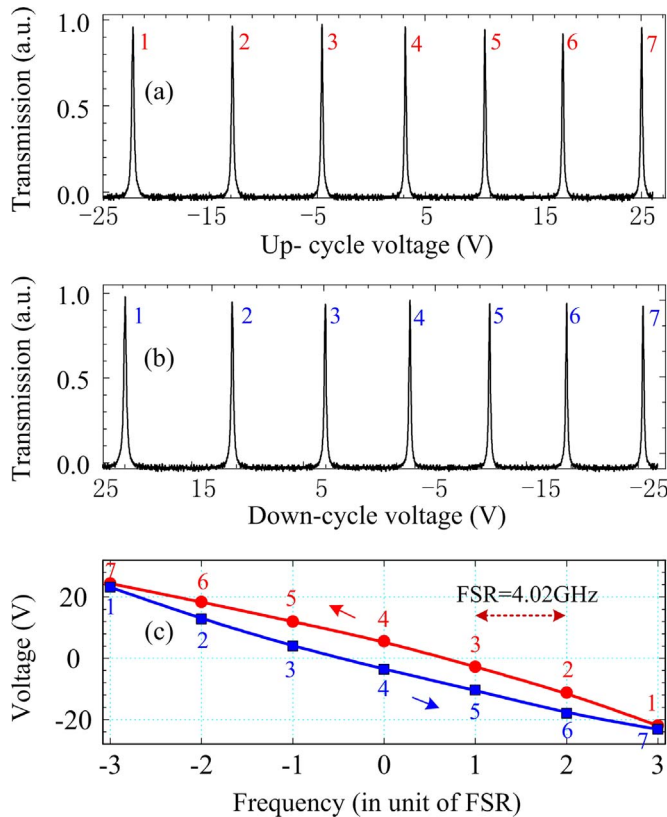


Fig. 2. Calibration of the fiber Fabry-Perot interferometer: transmission recorded on an oscilloscope as function of (a) the increasing voltage and (b) the decreasing voltage. (c) Measured hysteresis loop of the PZT.

divergence negligible in the cavity, thus its transmission is approximated to a Lorentzian function [15]:

$$h(v) = T_0/[1 + v^2/(\Delta v_{FPI})^2], \quad (2)$$

where $T_0 = 59.6\%$ is the peak transmission in this work, Δv_{FPI} is the FWHM of the transfer function. Finally, the transmission function

of the Brillouin signal through the FFP-SI is a convolution of Eqs. (1) and (2), yields,

$$T(v_R) = T_0/[1 + v_R^2/(\Delta v_B + \Delta v_L + \Delta v_{FPI})/2]^2, \quad (3)$$

where v_R is defined as the relative frequency of the FFP-SI to the Brillouin frequency center. Eq. (3) indicates that, once the transmission curve is obtained, the Brillouin frequency shift, power, and bandwidth can be retrieved simultaneously.

As free-run photon-counting acquisition is adopted, and back-scattering traces are time-gated and averaged for N independent shot times on the multiscaler, the optical signal to noise ratio is [16]

$$SNR = \frac{\eta}{hv_0} p(z, v_R) N \Delta t / \left(\frac{\eta}{hv_0} p(z, v_R) N \Delta t + D N \Delta t \right), \quad (4)$$

where z is the distance along the sense fiber, η is the quantum efficiency, h is the Planck constant, v_0 is the optical frequency of the signal, and Δt is the bin width of the multiscaler, which is set equal to the duration of the probe pulse, D is the dark count rate, $p(z, v_R)$ is the backscattering optical power from distance of z along the 9 km fiber for a single pulse [5]:

$$p(z, v_R) = p_0 R_B T(v_R) \exp(-2az), \quad (5)$$

where p_0 is the peak power of the probe pulse, $R_B = S \alpha_B v \Delta t / 2$ is the Brillouin backscattering factor, $\alpha_B = 7.1 \times 10^{-30} / \lambda^4$ is the Brillouin scattering coefficient at room temperature, S is the backscattering recapture factor given by $(\lambda/\pi n w)^2 / 4$, $w = 4.5 \mu\text{m}$ is the mode field radius of the fiber $n=1.453$ is the reflective index of the fiber core, $a = a_{dB}/4343$ is the fiber loss, where $a_{dB} = 0.3 \text{ dB/km}$ in this work.

Using the system parameters listed in Table 1, one can estimate the signal power $p(9000, 0) = 7.9 \times 10^{-11} \text{ W}$. Given the energy of single photon $E_0 = hv_0 = 1.28 \times 10^{-19} \text{ J}$, one can see that, $\eta p(z, 0)/hv_0 \gg D$ is satisfied along the whole 9 km sensing fiber. By assuming $SNR=1$, one can calculate the minimum detectable power (MDP) from Eq. (4), as

$$p_d = hv_0 [1 + (1 + 4DN\Delta t)^{1/2}] / 2\eta N \Delta t \quad (6)$$

Using system parameters $D = 40 \text{ cps}$ and $\Delta t = 20 \text{ ns}$, the photon-counting MDP for single-pulse detection is calculated as

$$p_d = hv_0 / \eta \Delta t. \quad (7)$$

A point worth emphasizing is that the above expression is exactly as the same as the ideal heterodyne MDP described as

$$p'_d = hv_0 B / \eta, \quad (8)$$

where $B = 1/\Delta t$ is defined as the bandwidth of the heterodyne receiver. The most valuable feature of photon-counting BOTDR is related to the potential for noiseless detection, through using detectors with low-noise and high quantum efficiency, according to Eq. (7). Whereas, for coherent BOTDR, shot-noise of local oscillator always exists, even in the absence of Brillouin backscatter. In other words, the up-conversion photon-counting detector can detect weak signals as low as the heterodyne detector. However, it is worth to mention that, APD based photon-counting detection is inferior to PIN diode based heterodyne detection at stronger signal powers. Thus, to achieve photon-counting BOTDR over long distance ($\sim 100 \text{ km}$), the peak power of the probe pulse needs to be enhanced to maintain an adequate SNR in the far end, while the near-field backscattering must be attenuated to avoid saturation due to the limited maximum count rate.

4. Experiment

The great challenge of this work is to manufacture and control

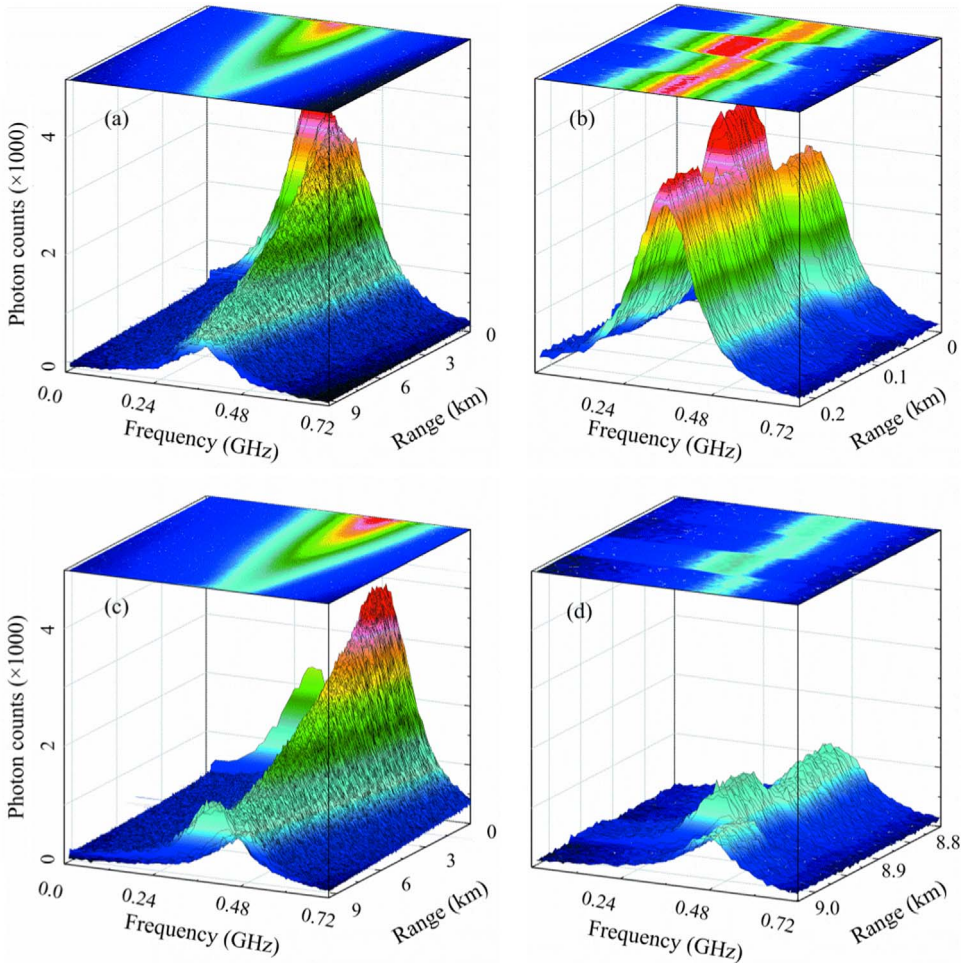


Fig. 3. (a) Brillouin spectra of unstrained PMF when the probe pulse lunched from the leading end. (b) Zoom-in image of (a) from 0 to 0.2 km. (c) Brillouin spectra when the probe pulse lunched from the trailing end. (d) Zoom-in image of (c) from 8.8 to 9 km.

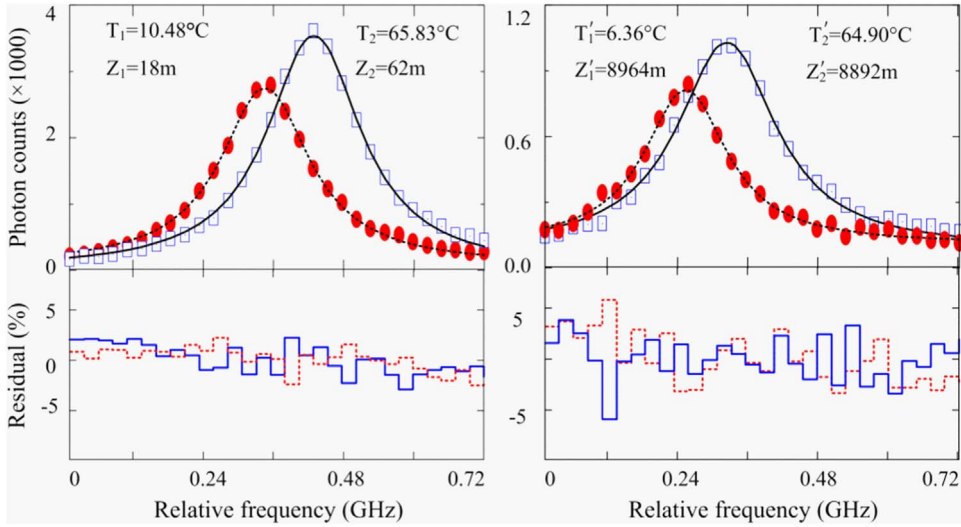


Fig. 4. Nonlinear fitting of the raw data to Lorentz functions at different ranges. Residuals are relative to the peaks.

the FFP-SI with high resolution and high stability transmission. We have experiences in using free-space Fabry–Perot interferometers for temperature lidar and Doppler wind lidars [17–19]. To eliminate the parallelism error of the reflecting mirrors during the

cavity scanning and the mode-dependent spectral broadening due to its illuminating condition, sophisticated electrical and optical techniques are required. In this work, to conquer these drawbacks, a lensless, plane Fabry–Perot interferometer is developed. The

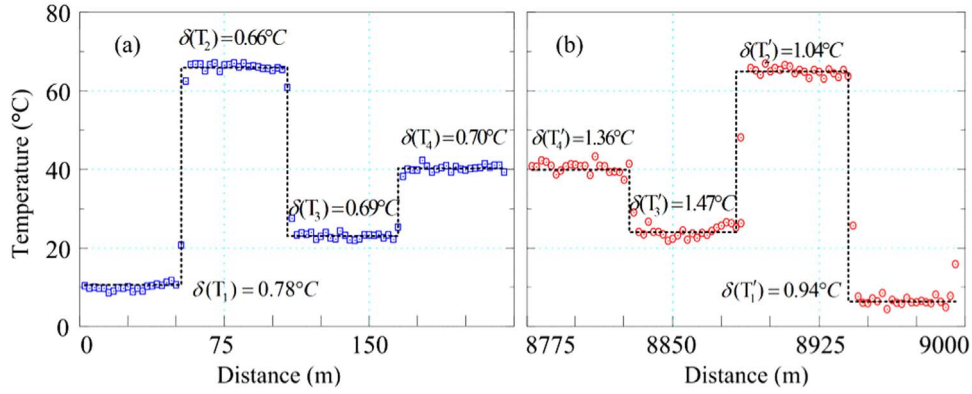


Fig. 5. Measured temperature profiles along the fiber, with standard deviation labeled in each section.

cavity is formed by two highly reflective multilayer mirrors that are deposited directly onto two carefully aligned optical fiber ends [20]. Frequency scanning of the FFP-SI is achieved by scanning the cavity length, as we introduced in detail in the Doppler wind lidar [19]. Here, only one piece of stacked piezoelectric transducer (PZT) is used to axially strain a short length of single-mode fiber that inserted in the cavity. The anti-reflection coated fiber inserted in the cavity provides confined light-guiding and eliminates secondary cavity.

One problem must be considered before the detection is the hysteresis introduced by the PZT. Fortunately, it is a repeatable phenomenon, which can be calibrated in the initialization process. As shown in Fig. 2, by changing the voltage (1 mV resolution, 1 μV accuracy) fed to the PZT, the transmission curve for a monochromatic CW laser over 7 interference orders are recorded using an oscilloscope on the up-cycle (increasing voltage) and on the down-cycle (decreasing voltage). The voltage values corresponding to every transmission peak is searched and tagged, as shown in Fig. 2.

In the frequency domain, the transmission of an FPI is periodic with a constant free spectral range (FSR). In the calibration process, a broadband light from an amplified spontaneous emission (ASE) source is fed to the FFP-SI without voltage added to the PZT. The FSR can be read out as 4.02 GHz from an optical spectrum analyzer (YOKOGAWA, AQ6370C) directly. Then, the peak voltage values on either up or down cycle of the scanning can be mapped into the frequency domain, as shown in Fig. 2(c). Nonlinear data fitting of the peak values on the up cycle and the down cycle to a 3-order polynomial function, respectively, forms the hysteresis loop of the PZT. Finally, the inherently non-linear cavity scanning due to hysteresis can be compensated in the data processing.

Thanks to the ultra-narrow passband (8 pm) and high sideband suppression (35 dB) of the temperature tunable FBG₂, the anti-Stokes Brillouin spectra along the PMF is picked out for temperature detection in the following experiments. The Brillouin spectra are scanned over 720 MHz with a sampling interval of 24 MHz per stage. At each sampling stage, the backscattering signal is accumulated over 0.5 s along the sensing fiber and gated in different range bins. The whole data acquisition time, i.e., the temporal resolution is 15 s.

As shown in Fig. 1, the probe pulse is injected from point (a) at the leading end in the first experiment. There are four sections of PMFs (YOFC, PM1047-C) in cascade, passing through different chambers set at different temperatures. The experiment results are plotted in Fig. 3(a), with a zoom-in image shown as Fig. 3(b). Changes in the Brillouin spectra due to temperature differences are observed apparently. To investigate the new technique quantitatively, the probe pulse is launched into the sensing fiber from the trailing end (point (b)) in the second experiment. The recorded

spectra are plotted in Fig. 3(c), also with a zoom-in image shown as Fig. 3(d). Due to the round-trip attenuation of the 9 km fiber, the signal-to-noise ratio in Fig. 3(d) is about 6 dB lower than that in Fig. 3(b).

In a calibration process, the temperature coefficients of frequency shift and power change are measured to be $a_1 = 1.46 \text{ MHz}/^\circ\text{C}$ and $a_2 = 0.63\%/\text{ }^\circ\text{C}$. Then the frequency shift and power fluctuation due to temperature can be retrieved by nonlinear fitting of the raw data to a Lorentz function with a Levenberg–Marquardt method. Nonlinear fitting results with residuals at different fiber locations are shown as examples in Fig. 4.

Finally, the temperature values in both Fig. 3(b) and (d) are retrieved according to the frequency shift of the Brillouin spectra. The measured temperature values are plotted in Fig. 5, with standard deviation estimated in each section. The precision of temperature detection is about 0.7 °C at the leading end and 1.2 °C at the trailing end.

5. Conclusion

We demonstrated a direct-detection BOTDR based on an up-conversion photon-counting detector and a scanning Fabry–Perot interferometer with all-fiber structure. The Brillouin gain spectra along a 9 km polarization maintaining fiber are analyzed in the optical domain directly. Similar to the heterodyne BOTDR, photon-counting BOTDR can also achieve a shot-noise limited detection of the weak Brillouin backscattering from the sensing fiber. Obviously, the data volume of photon-counting BOTDR is smaller than that in the heterodyne BOTDR, shortening the time costed in data transferring and processing.

In developing the next generation up-conversion photon-counting detector, we will continue to enhance the detection efficiency and suppress the dark count rate. And we point out that, using up-conversion technique [13] and edge technique [19], one can realize distributed dynamic strain detection, since no time-consuming frequency scanning is needed anymore.

Acknowledgments

This work has been supported by the National Natural Science Foundation (41274151 and 41421063), the CAS Hundred Talents Program (D), the CAS Program (KZZD-EW-01-1), the National Fundamental Research Program (2011CB921300 and 2013CB336800), and the 10000-Plan of Shandong Province.

References

- [1] X. Bao, L. Chen, Recent progress in Brillouin scattering based fiber sensors, *Sensors* 11 (2011) 4152–4187.
- [2] X. Bao, J. Dhliwayo, N. Heron, D.J. Webb, D.A. Jackson, Experimental and theoretical studies on a distributed temperature sensor based on Brillouin scattering, *J. Lightwave Technol.* 13 (1995) 1340.
- [3] T. Kurashima, M. Tateda, T. Horiguchi, Y. Koyamada, Performance improvement of a combined OTDR for distributed strain and loss measurement by randomizing the reference light polarization state, *IEEE Photon. Technol. Lett.* 9 (1997) 360.
- [4] T.R. Parker, M. Farhadiroushan, R. Feced, V.A. Handerek, A.J. Rogers, Simultaneous distributed measurement of strain and temperature from noise-initiated Brillouin scattering in optical fibers, *IEEE Quantum Electron.* 34 (1998) 645.
- [5] T. Horiguchi, K. Shimizu, T. Kurashima, M. Tateda, Y. Koyamada, Development of a distributed sensing technique using Brillouin scattering: optical fiber sensors, *J. Lightwave Technol.* 13 (1995) 1296.
- [6] E. Geinitz, S. Jetschke, U. Ropke, S. Schroter, R. Willsch, H. Bartelt, The influence of pulse amplification on distributed fibre-optic Brillouin sensing and a method to compensate for systematic errors, *Meas. Sci. Technol.* 10 (1999) 112.
- [7] M. Ali, M. Belal, T.P. Newson, Distributed dynamic large strain optical fiber sensor based on the detection of spontaneous Brillouin scattering, *Opt. Lett.* 38 (2013) 3312.
- [8] C. Boller, W.J. Staszewski, Aircraft structural health and usage monitoring, *Health Monitoring of Aerospace Structures*, Wiley, New York, 2003.
- [9] Q. Cui, S. Pamukcu, A. Lin, W. Xiao, D. Herr, J. Toulouse, M. Pervizpour, Distributed temperature sensing system based on Rayleigh scattering BOTDA, *IEEE Sensors J.* 11 (2011) 2.
- [10] L. Xia, J. Hu, Q. Zhao, J. Chen, P. Wu, X. Zhang, A distributed Brillouin temperature sensor using a single-photon detector, *IEEE Sensors J.* 16 (2016) 7.
- [11] R.H. Hadfield, Single-photon detectors for optical quantum information applications, *Nat. Photon.* 3 (2009) 696.
- [12] F. Marsili, V.B. Verma, J.A. Stern, S. Harrington, A.E. Lita, T. Gerrits, I. Vayshenker, B. Baek, M.D. Shaw, R.P. Mirin, S.W. Nam, Detecting single infrared photons with 93% system efficiency, *Nat. Photon.* 7 (2013) 210–214.
- [13] H. Xia, G. Shentu, M. Shangguan, X. Xia, X. Jia, C. Wang, J. Zhang, J.S. Pelc, M. M. Fejer, Q. Zhang, X. Dou, J. Pan, Long-range micro-pulse aerosol lidar at 1.5 m with an up-conversion single-photon detector, *Opt. Lett.* 40 (2015) 1579–1582.
- [14] E. Patrick, M. Legr, J. Zhang, H. Zbinden, N. Gisin, Photon counting OTDR: advantages and limitations, *J. Lightwave Technol.* 28 (2010) 952.
- [15] H. Xia, C. Zhang, H. Mu, D. Sun, Edge technique for direct detection of strain and temperature based on optical time domain reflectometry, *Appl. Opt.* 48 (2009) 189–197.
- [16] P. Healey, Optical time domain reflectometry – a performance comparison of the analogue and photon counting techniques, *Opt. Quantum Electron.* 16 (1984) 267–276.
- [17] H. Xia, X. Dou, M. Shangguan, R. Zhao, D. Sun, C. Wang, J. Qiu, Z. Shu, X. Xue, Y. Han, Y. Han, Stratospheric temperature measurement with scanning Fabry–Perot interferometer for wind retrieval from mobile Rayleigh Doppler lidar, *Opt. Express* 22 (2014) 21775–21789.
- [18] H. Xia, X. Dou, D. Sun, Z. Shu, X. Xue, Y. Han, T. Cheng, Mid-altitude wind measurements with mobile Rayleigh Doppler lidar incorporating system-level optical frequency control method, *Opt. Express* 20 (2012) 15286–15300.
- [19] H. Xia, D. Sun, Y. Yang, F. Shen, J. Dong, T. Kobayashi, Fabry–Perot interferometer based Mie Doppler lidar for low tropospheric wind observation, *Appl. Opt.* 46 (2007) 7120–7131.
- [20] H. Venghaus, *Wavelength Filters in Fiber Optics*, Springer, Berlin, 2006.